Dry granular collapse into a liquid: Role of viscous dissipation on granular flow regimes and associated waves

Alexis Bougouin, Sylvain Viroulet, Laurent Lacaze, Olivier Roche, Raphaël Paris

Dry granular collapse into a liquid: Role of viscous dissipation on granular flow regimes and associated waves

Alexis Bougouin

Dipartimento di Ingegneria Informatica, Modellistica, Elettronica e Sistemistica, Università della Calabria, 87036 Rende, Cosenza, Italy

Sylvain Viroulet* and Laurent Lacaze

Institut de Mécanique des Fluides de Toulouse (IMFT), Université de Toulouse, CNRS-INPT-UPS, Toulouse, France

Olivier Roche and Raphaël Paris

Laboratoire Magmas et Volcans, Université Clermont Auvergne, CNRS, IRD, OPGC, 6 Avenue Blaise Pascal, Clermont-Ferrand, France

(Dated: December 6, 2024)

Abstract

This study investigates the role of grain-fluid interactions, and especially those related to viscous dissipation, in the generation process of landslide tsunamis. For this purpose, original laboratory experiments on the collapse of a dry granular mass into a liquid are presented, in which only the grain size and liquid viscosity are varied to modify grain-scale viscous dissipation. By following the temporal evolution of the granular and free-surface height profiles, our results first reveal a surprising wealth in dynamics of granular collapses entering the liquid. Three distinct regimes are identified, namely dense-inertial, dilute-inertial and dense-viscous regimes. These regimes are described in terms of the flow Reynolds number Re and the Stokes number St that prescribe the relative importance of flow and particle inertia, respectively, to viscous dissipation of the liquid. Whereas the two inertial regimes are characterized by relatively fast and far propagation of, either dense or dilute, granular flows once immersed, the dense-viscous regime consists of the sudden arrest of the granular material on the incline, possibly accompanied by lift-off from the front. Although the collapse dynamics and deposition are very different for each of these regimes, they barely affect the first and largest wave, which suggests that (i) the generation of the leading wave is mainly governed by the impact process depending on subaerial flow conditions, and (ii) large-amplitude waves are not necessarily associated with long depositional runouts. In fact, granular flow regimes contribute mainly to the total energy transferred to the free surface and the resulting wave train, rather than only the leading wave. Accordingly, we show that the leading wave to total wave train energy ratio follows a master curve depending only on St, for dense granular flow regimes. Altogether, these results help to understand better physical mechanisms involved in landslide-tsunami generation, for which St can varied significantly at large Re, while offering an original and relevant benchmark for numerical models.

I. INTRODUCTION

Particulate-laden flows are encountered in many geophysical processes, such as rockfalls, landslides, pyroclastic flows and snow avalanches [1]. When such events occur near the sea, a lake or a river, granular avalanches may reach water and interact with it, eventually

* sylvain.viroulet@imft.fr

leading to the generation of impulse waves. Despite this, the physical processes involved in the transient dynamics from dry to immersed granular flows are not well understood yet.

The configuration of a dry granular material penetrating water has mainly been approached with the aim of improving the modeling of landslide tsunamis [2–9]. The sliding modeling by a granular material has the advantage to take into account the deformability, compressibility, and porosity of granular media [5, 8, 10–12], which are not considered with rigid blocks [13–18]. More specifically, 2D configurations of granular collapses [4, 9, 19–22] and granular flows [2, 3, 6–8, 23, 24] released into the water have been intensively studied through laboratory experiments and numerical simulations, for which the properties of the leading wave were characterized from the flow conditions. Several studies conclude that the Froude number $Fr = u_s/(gH_o)^{1/2}$, comparing the slide velocity u_s with the typical velocity of small-amplitude waves in shallow water, where g is the gravitational acceleration and H_o is the still water depth, is the key parameter governing wave generation [9, 21, 23, 25, 26], as already reported in seminal work considering rigid blocks [15]. Based on a momentum transfer approach, other studies show that the Froude number can also be rewritten in terms of the slide-to-water height and density ratios [20, 27, 28]. Finally, more complex empirical relationships based on correlations from a large number of experiments have also been proposed to predict the features of waves generated [2, 3, 6, 8]. Beyond the Froude number Fr, these relationships include other dimensionless parameters as the relative slide thickness S, the relative mass M, and the slope angle θ of the inclined plane. However, the use of these empirical laws may lead to significant inaccuracies in the prediction of wave features, while there is still a lack of physical understanding [29].

Whichever approach is chosen, it remains difficult to provide a unique law to predict the characteristics of the waves, suggesting that other physical processes are missing. In particular, most of the proposed laws include only parameters at the flow scale, while the grain scale is usually disregarded. Some studies conclude that grain properties do not affect significantly wave generation [3, 9, 22], but others show the opposite by attributing it to the ability of water to percolate through the porous granular medium [5, 8, 11, 20] or to the granular kinematics beneath the water surface [30]. The underwater dynamics of initially subaerial granular flows is also strongly influenced by grain size, which in turn plays a role in the formation of secondary waves. Laboratory experiments using volcanic ash flows [31, 32] and submillimetre grain flows [8, 24, 33] impacting water show that particle-driven

gravity currents are formed underwater and propagate far away. In contrast, millimetric and centimetric grains entering the water result in dense granular flows that slow down rapidly and form thick deposits at the slope break [4, 7, 9, 34]. Finally, the key role of local processes at the dry-to-wet transition of granular materials has already been reported in other flow configurations, such as granular jets penetrating a water bath [35, 36]. It is therefore pertinent to ask how the grain-liquid interplay affects the collapse dynamics and deposition of a dry granular mass entering water, and the associated wave generation. This is especially crucial given that grain size can vary by several orders of magnitude, from micrometers to tens of meters, in nature [1].

The aim of the present study is to characterize the influence of grain-scale processes, particularly those related to viscous dissipation, on the dynamics of a granular medium entering a liquid pool, and on the resulting waves. For that purpose, we perform original laboratory experiments on the collapse of a dry granular mass into a liquid by varying both grain size and liquid viscosity, while other previously studied parameters are kept constant. The variation in grain size and liquid viscosity permits us to investigate a wide range of grain-scale viscous dissipation that can be encountered in nature, while avoiding misinterpretation of the results. The paper is organized as follows. In Sec. II, the experimental apparatus, materials and relevant dimensionless parameters are introduced. Then, Sec. III describes the wealth of granular collapse regimes observed, which are then rationalized in the (Re, St) plane. Finally, Secs. IV and V are dedicated to wave structure with regard to granular flow regimes.

II. EXPERIMENTAL SETUP

A. Apparatus and materials

The experimental setup is based on previous studies of laboratory configurations for studying impulse wave generation by impact of granular collapses [4, 11, 20, 25, 30, 37]. These studies have already reported the role of several parameters on the wave amplitude, including the Froude number, or equivalently the slide-to-water height and density ratios. Here, we describe a similar apparatus, in which these parameters are held constant to deal more specifically with the role of viscous dissipation, from the dimensionless parameters

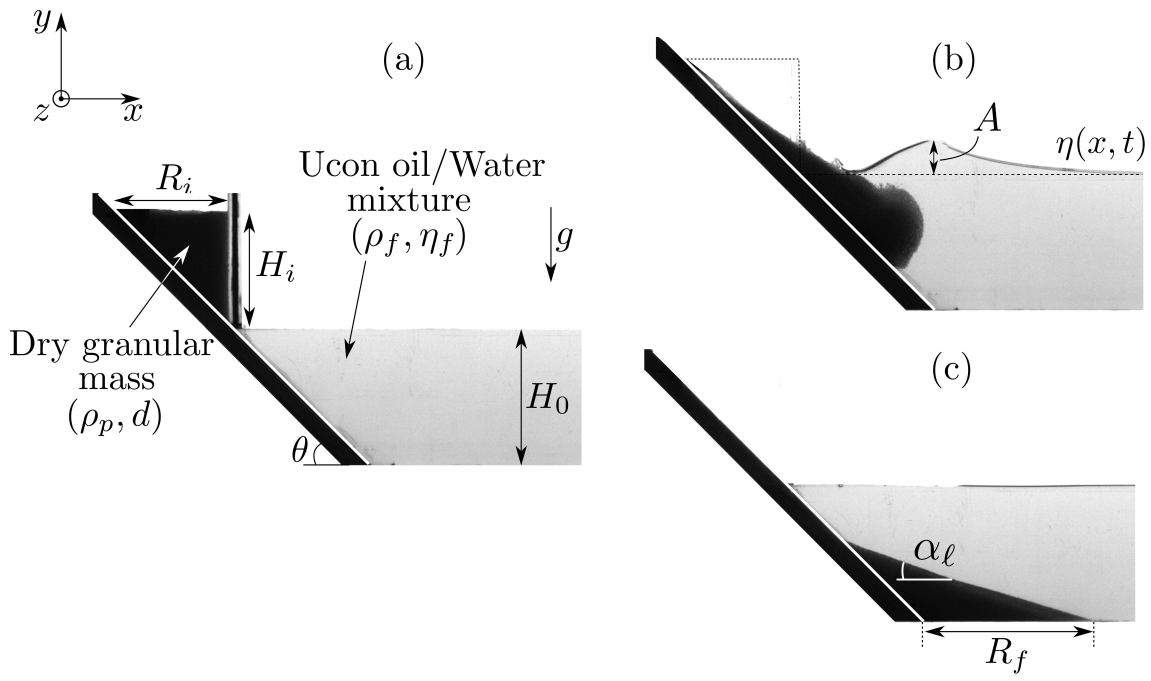

FIG. 1. Collapse of dry glass beads ($d = 1$ mm) into a viscous fluid ($\rho_f = 1014\,\mathrm{kg.m^{-3}}$, $\eta_f = 9\,\mathrm{mPa.s}$), at (a) the initial time before opening the gate, (b) a given time during the collapse, and (c) a long time when the final deposit is formed.

described later (Sec. II B).

The experimental apparatus consists of a horizontal, transparent, rectangular cross-section channel of 2 m long, 0.35 m high and 0.2 m wide along the longitudinal x, vertical y and spanwise z directions, respectively (Fig. 1). The channel is filled up to a height $H_o = 14.5 \pm 0.5$ cm with a mixture of water and Ucon oil 75H90000 (a viscous Newtonian fluid soluble in water). The properties of the mixture depend on the mass fraction $c_m = m_o/(m_o + m_w)$, with m_o and m_w the mass of oil and water, respectively. In this study, five different mixtures ranging from $c_m = 0$ to 30% are used, corresponding to liquid density, dynamic viscosity and surface tension ranging from $\rho_f = 1000$ to $1047\,\mathrm{kg.m^{-3}}$, $\eta_f = 1$ to $126\,\mathrm{mPa.s}$, and $\sigma_f = 0.07$ to $0.05\,\mathrm{N.m^{-1}}$, respectively. The density is measured using a DMA 35 Anton Paar electronic densimeter with an accuracy of $\pm 0.5\,\mathrm{kg.m^{-3}}$, the dynamic viscosity is obtained by rheometric measurements using a cone plate in a Haake Mars III rheometer with an accuracy of 5%, and the surface tension is extracted from a calibration curve of previous measurements performed with an electronic tensiometer DSA 100 with an

accuracy of 5% (more details are given in Ref. [38]).

On one side of the channel, a granular mass of $m = 2\,\mathrm{kg}$ is initially maintained by a vertical gate just above the undisturbed free surface on a smooth plane inclined at an angle of $\theta = 45°$ (with respect to the horizontal). The granular mass is preserved in the random packing configuration, i.e. without compaction, corresponding to an initial height and an initial volume fraction of $H_i = 11.6 \pm 0.3\,\mathrm{cm}$ ($\equiv R_i = H_i/\tan\theta$, with R_i the initial length) and $\phi \approx 0.6 \pm 0.03$, respectively. The granular material is composed of quasi-monodisperse and spherical glass beads of density $\rho_p = 2500\,\mathrm{kg.m^{-3}}$, while the mean diameter is varied over two orders of magnitude, from 55 μm to 16 mm with intermediate diameters. Beyond the changes in grain-liquid interactions, the increase in grain size also reduces basal and internal friction. To help interpretation of the results, the characteristics of the deposits are always compared with those obtained by releasing a mass of the same grains on the bottom without inertia, referred to in the following as quasistatic granular collapse (Appendix A). A summary table of the experiments is provided in Ref. [39].

At the initial time $t = 0$, the vertical gate is removed manually in about 0.1 s and the dry granular material collapses along the inclined plane into the liquid. The opening time is lower than the free-fall timescale $T_{FF} = (2H_i/g)^{1/2}$, which ensures that the initial condition does not affect significantly the granular dynamics [21, 40]. Using a shadowgraphy method, the temporal evolution of the disturbed free surface and the granular flow are recorded with a Basler 2000×2000 pixel camera. The spatial resolution is $525\,\mu$m/pixel, and the acquisition rate is varied from 50 to 250 Hz depending on the collapse dynamics.

B. Dimensional analysis

This study aims to investigate the role of grain-liquid interactions, and more specifically those related to viscous dissipation, on the dynamics of a dry granular mass entering a liquid and the resulting waves. In the present study, the grain size and liquid viscosity are systematically varied and we identify in the following the relevant dimensionless parameters.

At the grain scale, the relative importance of grain inertia over viscous dissipation can be quantified through the Stokes number $St = [\rho_p(\rho_p - \rho_f) g \sin\theta d^3]^{1/2}/18\sqrt{2}\eta_f$, whose definition follows several studies on immersed granular flows [41, 42]. In this study, it is varied in the range of $St = [2 \times 10^{-3} : 4 \times 10^2]$, which is included in the wide range $St = [10^{-4} : 10^6]$ of

natural materials that can interact with water [1]. According to these studies [41, 42], the grain-fluid density ratio is also defined as $r = (\rho_p/\rho_f)^{1/2} \sim 1.5$. Note that both St and r can also be defined on the basis of a typical propagation length of grains, thus taking into account both grain and flow scales [42]. However, this leads to more complex definitions of the couple (St, r) without helping further in the analysis that follows. Then, the variation in grain size also modifies capillary effects at the interface between the interstitial air and the surrounding liquid. Such effects can be quantified by the Bond number $Bo = \rho_p g d^2/\sigma_f$, which is varied from 10^{-3} to 10^2. Capillarity could therefore affect quantitatively the following results and could be the object of further study, but the Stokes number St will be shown to be predominant in this study.

At the macroscopic scale, the initial granular mass is characterized by the aspect ratio $a = H_i/R_i$ and the volume fraction of grains, both fixed at $a = 1$ and $\phi \approx 0.6 \pm 0.03$, respectively. Based on similar description of the fluid-grain dynamics providing the Stokes number St at the grain scale (see Refs. [41, 42] for the details), a macroscopic Reynolds number (at the scale of the granular flow) is defined as $Re = [\rho_f(\rho - \rho_f)g \sin\theta H_i]^{1/2} H_i/\eta_f$, where $\rho = \phi\rho_p + (1-\phi)\rho_a$ and $\rho_a = 1.2\,\mathrm{kg.m^{-3}}$ are the densities of the initial granular mass and of the ambient air, respectively. Here, the flow Reynolds number is found in the range of $Re = [6 \times 10^2 : 7 \times 10^4]$, while it is expected to be relatively high in the field as $Re \propto (H_i/d)^{3/2} St = [10^4 : 10^7]$, i.e. small St implies large H_i/d.

Finally, the wave generation is associated with a Froude number $Fr = (2H_i/H_o)^{1/2} \sim 1$, which assumes a typical slide velocity $(2gH_i)^{1/2}$ of an inertial slumping and a typical wave velocity $(gH_o)^{1/2}$ of small-amplitude waves in shallow water. In the framework of previous studies on amplitude of landslide tsunamis, keeping Fr constant in our experiments means that the generated waves should be the same, over the full range of parameters considered [9, 21, 25, 26].

III. GRANULAR COLLAPSE REGIMES

At $t = 0$, the sluice gate is rapidly removed and the grains collapse down the incline, pushing the liquid. By varying only the grain size and liquid viscosity, qualitative observations first reveal significant differences in granular dynamics and deposition below the liquid surface (Fig. 2, see also movies [43–47]), which are detailed below.

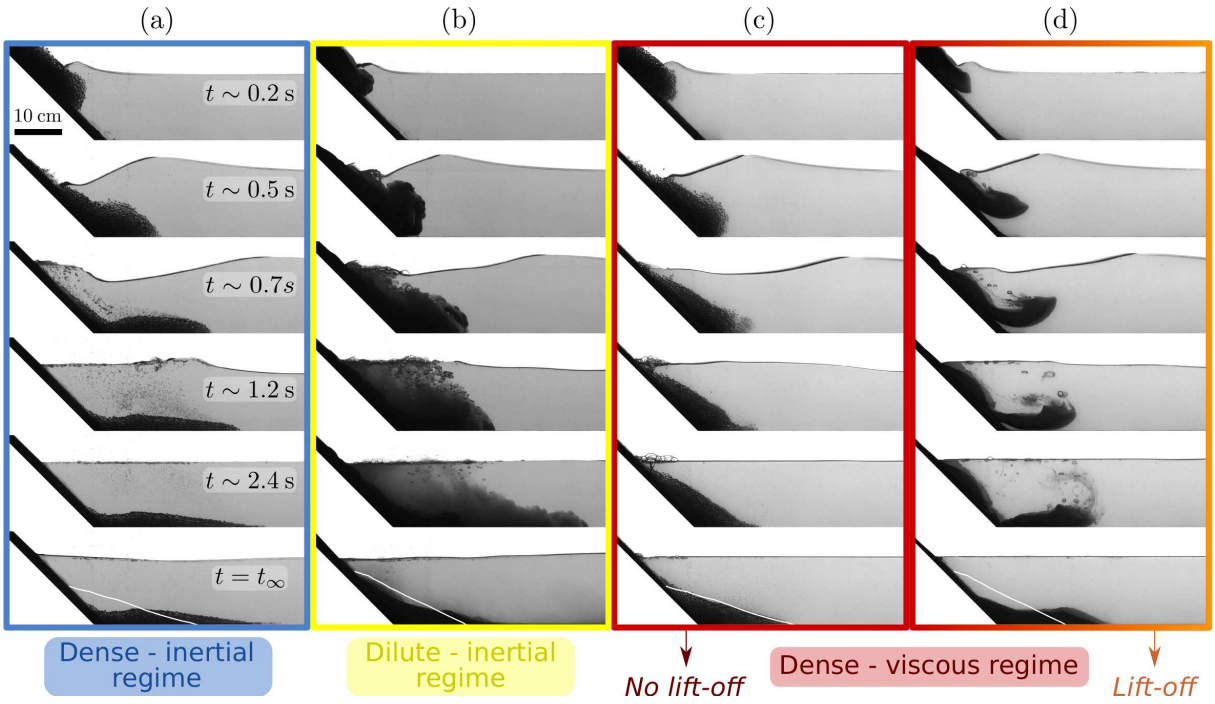

FIG. 2. Snapshots of a dry granular collapse into a liquid: (a) $d = 5$ mm, $\eta_f = 1$ mPa.s, (b) $d = 120\,\mu$m, $\eta_f = 1$ mPa.s, (c) $d = 5$ mm, $\eta_f = 126$ mPa.s, and (d) $d = 120\,\mu$m, $\eta_f = 126$ mPa.s. At $t = t_\infty$, white solid lines are deposits for quasistatic granular collapses (more details in Appendix A).

When d is large and η_f is small enough (Fig. 2(a) and movie 1 [43]), the granular mass spreads densely and rapidly over the immersed bottom plane, before reaching its final state. At some point after the granular material has entered the liquid pool, initially trapped air bubbles are released from the granular matrix and rise up to the liquid surface. The release of air bubbles from the granular material mostly stands during the entire avalanche dynamics until reaching the deposit. Furthermore, grain inertia promotes a mass transfer from the tail to the front of the flow along the horizontal plane, forming a nonmonotonous and elongated deposit, as already reported for other collapsing configurations of large grains in water [7, 34, 42]. More specifically, the deposit is characterized by a runout longer than that of quasistatic granular collapses [white solid line, Fig. 2(a)], while it is expected to be lower than inertial ones obtained for fully dry and immersed cases [4, 7, 34]. From here on, this collapse regime will be referred to as *dense-inertial regime*.

As d decreases (Fig. 2(b) and movie 2 [44]), fluid flow inertia promotes dilation of the

granular medium characterized by a current head thickening and a significant outgassing. This results in the formation of a dilute particle-laden current that propagates away and deposits a thin granular layer along the horizontal plane. In addition, a thick granular mass is also deposited at the slope break, meaning that not all grains were suspended. Such a behavior is commonly reported for the entry of fine-grained granular flows into water [8, 24, 32, 33, 48], and it is referred to as *dilute-inertial regime*.

When viscous dissipation are predominant at both grain and flow scales (Figs. 2(c) and 2(d), movies 3 and 4 [45, 46]), i.e., for small d and large η_f, singular and never-before-reported dynamics of granular flows are observed. Avalanches occur on a much longer timescale than the two above-mentioned inertial regimes. Once the granular material has fully entered the liquid, it is quickly either completely stopped on the incline [Fig. 2(c)], or partially stopped with the frontal part detaching and lifting off the incline before falling in mass away [Fig. 2(d)]. In both cases, a somehow significant similarity is the fact that the granular medium, remaining dense, is prevented to keep propagating along the slope on a finite time scale, either stopping or being reoriented into another direction, actually nearly horizontal. This sudden stop behavior on the incline can even be better observed by increasing the water height as the granular front is still far from the slope break (not shown here, see movie 5 [47]). Unexpectedly, the transient deposit has an apparent slope greater than the angle of repose of the granular material. This reveals stabilization by viscous additional stresses attributed to liquid percolation into the granular matrix, which is supported by local, quasistatic granular avalanches and slow air escape at the foot and summit, respectively, of the transient deposit. The mechanism of liquid percolation, and associated granular stabilization along the slope, is further discussed in Appendix B. Finally, the obtained final deposits have a maximum local slope equal to the angle of repose of granular materials, resulting from the quasistatic dynamics of local granular avalanches. In the absence of lift-off, the entire final deposit is even strictly equivalent to that of quasistatic granular collapses [white solid line, Fig. 2(c)]. In the following, this viscous-dominated collapse behavior is referred to as *dense-viscous regime*.

These three identified regimes - dense-inertial, dilute-inertial, and dense-viscous regimes - of granular collapse into a liquid result from unique variation in grain size and liquid viscosity. This is interpreted as the signature of the relative importance of flow inertia, grain inertia and viscous dissipation, which can be rationalized in the (Re, St) plane (Fig.

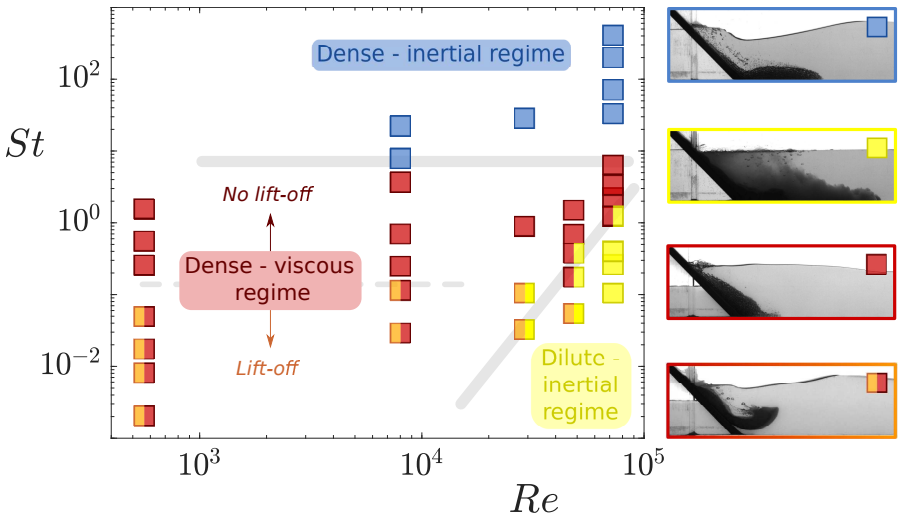

FIG. 3. Granular collapse regimes into a liquid, in the (Re, St) plane. Pictures, and corresponding symbols, show typical granular dynamics for each of the identified regimes. Red-yellow and orange-yellow squares correspond to experiments, for which one hardly differentiates between the two regimes.

3). For $St \gtrsim 10$ (and not too large Re), the liquid plays a minor role in the dynamics of the granular avalanche, corresponding to the dense-inertial regime. For $St \lesssim 10$, viscous effects become predominant at the grain scale that limit drastically liquid percolation into the densely-packed granular medium. The transition from the dense-inertial regime to the dense-viscous one is similar to that reported for fully immersed granular collapses [42], depending mainly on St, on either side of a critical value of $St \approx 10$ [41, 42]. This suggests that this transition involves the same physical processes between the two configurations, whereas the other transitions are only observed in the specific case of dry grains collapsing into a liquid. Thus the system adapts in different ways to liquid percolation at small St depending on Re. At large enough Re, the flow inertia causes significant dilation of the granular medium, more easily releasing air trapped and mixing with the liquid, corresponding to the dilute-inertial regime. At lower Re, however, the dense-viscous regime is characterized by collapse dynamics that is fully controlled by viscous dissipation at both the grain and flow scales. It prevents any percolation of liquid and dilation of the granular medium during collapse. When St is small enough, i.e., $St \lesssim 10^{-1}$, viscous effects are so important that the granular front cannot be deformed anymore, leading to a lift-off from the incline. Note that the

transition from the dense-viscous regime to the dilute-inertial regime is a combination of Re and St, reflecting a balance between flow and grain inertia. According to this regime map, the results are discussed in light of the Reynolds number Re and the Stokes number St in the following.

IV. AMPLITUDE VERSUS RUNOUT

Different granular flow regimes have been identified in the (Re, St) plane, whose collapse dynamics and deposit morphology differ greatly from one to another. Accordingly, one might expect that wave generation would also be strongly altered by them. However, the normalized maximum amplitude A/H_o of the leading and largest wave varies very little in the (Re, St) plane [Fig. 4(a)]. A maximum variation of $20\% - 25\%$ in amplitude is reported here by varying both Re and St over several orders of magnitude. This means that significant differences in collapse dynamics do not play a major role in the generation process of the leading wave, which can be concluded to be mainly controlled by subaerial flow conditions. This relatively low influence also contrasts sharply with the significant variation in the depositional runout R_f/R_f^s, which can vary by up to a factor of 2 [Fig. 4(b)]. Thus the deposit runout may not be a relevant quantity for providing an estimate of the amplitude of the leading and largest wave, at least for small Fr [23].

To strengthen this observation, both A/H_o and R_f/R_f^s are plotted as a function of St, in Figs. 4(c) and 4(d). Recall that the Stokes number St alone can describe most regime transitions, with the exception of the dilute-inertial regime, which is therefore ignored from now on (the dataset, available in Refs. [39, 44], is not sufficient to fully conclude on it). First, it can be clearly observed that the normalized amplitude A/H_o decreases slowly and monotonically with increasing St [Fig. 4(c)]. This contrasts with significant and nonmonotonic variations in the normalized runout R_f/R_f^s of deposits with St [Fig. 4(d)]. More specifically, R_f/R_f^s first decreases, then reaches a plateau such that the runout is the one of quasistatic granular collapses, and finally increases with increasing St. This nonmonotonous trend is consistent with the transitions of granular collapse regimes reported in Sec. III, given that the runout represents the final signature of the granular collapse dynamics. Altogether, this suggests that the wave amplitude is not correlated here to the granular dynamics, and therefore its final deposit. This highlights the need for caution when associating large runouts

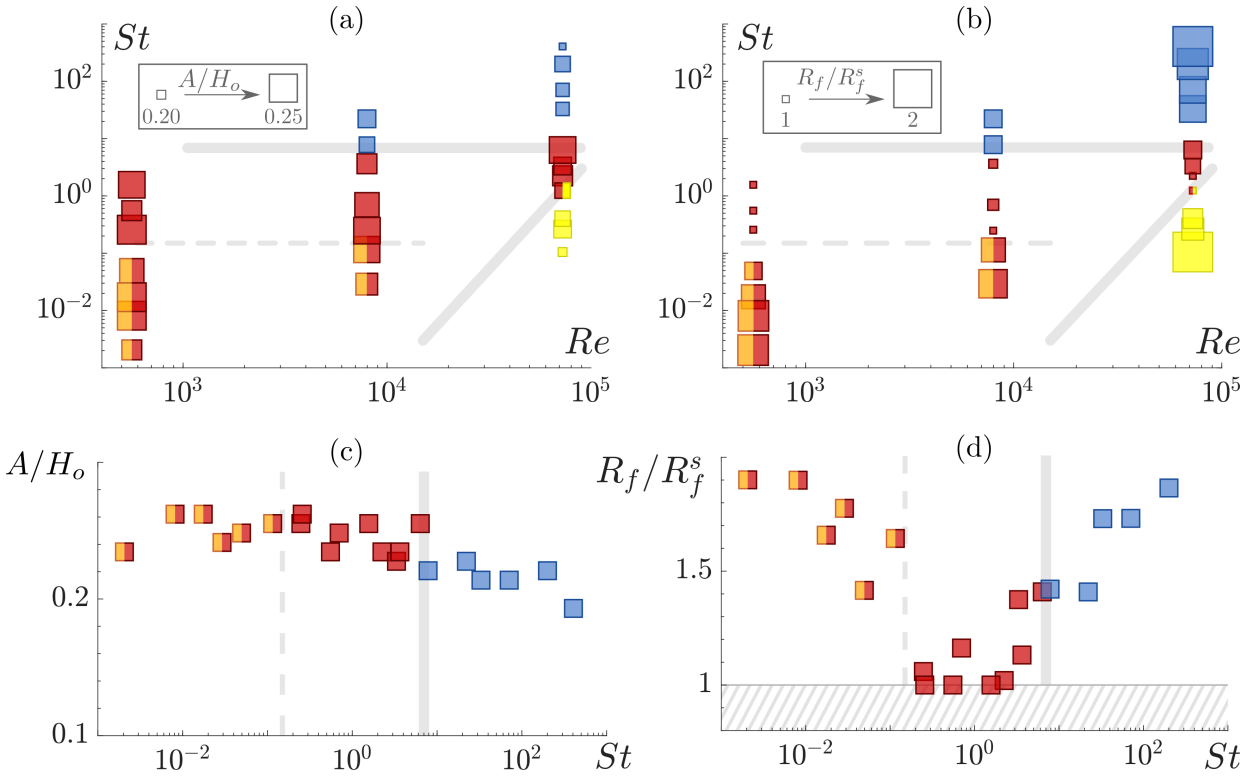

FIG. 4. (a) Normalized amplitude A/H_o and (b) normalized runout R_f/R_f^s in the (Re, St) plane. R_f^s is the runout of quasistatic granular collapses (Appendix A). For the dilute-inertial regime, R_f is largely underestimated and more representative of thick deposition at slope break because the thin layer deposited by the dilute current is not captured by the camera. Color and size of symbols indicate the granular collapse regime and the quantitative value, respectively [see the legends to Figs. 3, 4(a) and 4(b)]. (c) A/H_o and (d) R_f/R_f^s vs the Stokes number St.

with large-amplitude waves.

With the aim of providing deposit features that reflect the maximum amplitude of the leading wave, another observable is required. We propose here to focus on the maximum local angle α_ℓ of final granular deposits (see Fig. 1). Even if the latter is dependent on St (as discussed later), it does not follow the trend of identified granular flow regimes and associated runouts. In fact, it informs on local processes at the grain scale, which occur during the immersed collapse dynamics. In particular, one obtains that this normalized angle α_ℓ/α^s evolves monotonically and decreases with increasing St (inset, Fig. 5), as observed for the wave amplitude and unlike the deposit runout. Thus an increase of α_ℓ/α^s is associated with

an increase of A/H_o, both being related to a greater importance of viscous effects at the grain scale (Fig. 5). Furthermore, extrapolation of the trend of A/H_o with α_ℓ/α^s suggests that the wave amplitude is bounded between two limiting values, $A/H_o \approx 0.18$ and 0.27 for $\alpha_\ell/\alpha^s = 0$ and 1, giving here a maximum increase of up to 50% in wave amplitude (gray dashed line, in Fig. 5).

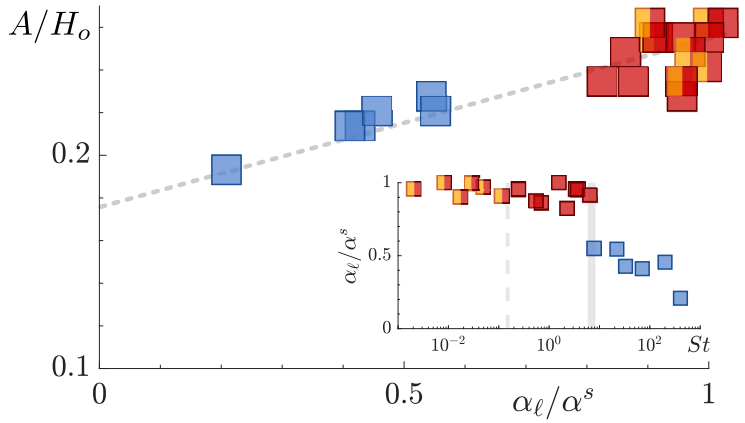

FIG. 5. Normalized amplitude A/H_o vs the maximum local angle α_ℓ of deposits, normalized by the depositional angle α^s obtained for quasistatic granular collapses (Appendix A). Inset: α_ℓ/α^s vs St. Legend of symbol colors is given in Fig. 3.

To conclude, the different granular collapse regimes do not play a major role in the generation of the leading and largest wave. The wave amplitude decreases slowly with increasing St, suggesting that wave amplitude is not at all correlated to the inertia of the global avalanche. This could rather be associated with liquid percolation [5, 8], which also depends on St, but whose associated flow rate through the porous granular medium is reduced as St decreases. This would therefore promote greater surface deformation, and then larger leading wave amplitude, with decreasing St. In such a scenario, it is shown that the maximum local angle of the deposit can reflect this mechanism as a reasonable correlation is obtained with the leading wave amplitude.

V. ENERGY TRANSFERS

In order to go a step further in the analysis of the generation process and to understand better the link between the identified granular collapse regimes and the wave structure, we

are now focusing on the temporal evolution of the entire wave train, rather than only the leading and largest wave. As shown previously, the Stokes number St is the most relevant parameter for describing dense granular flow regimes, i.e. dense-inertial and dense-viscous regimes, and it is therefore the only one to be considered in the following. Recall that the dilute-inertial regime is expected to depend on the couple (Re, St), and further studies should be dedicated to this specific and more complex situation. As it is, the dataset is not sufficient to fully conclude on the dependence of the dilute-inertial regime without speculating (data given in Refs. [39, 44]), being observed in a small region of the (Re, St) plane (typically, smallest grains in water).

Qualitatively, the temporal evolution of the free surface is shown to be strongly affected by the Stokes number St (Fig. 6). While the small variation in amplitude of the leading wave is barely observed, a significant difference is reported in the following wave train. At large St [Fig. 6(a)], the first trough and secondary waves have large amplitudes and are of the same order of magnitude as the leading wave. By contrast, at low St [Fig. 6(b)], the wave train that follows the leading wave is almost nonexistent. These observations suggest that inertia promotes the generation of a wave train.

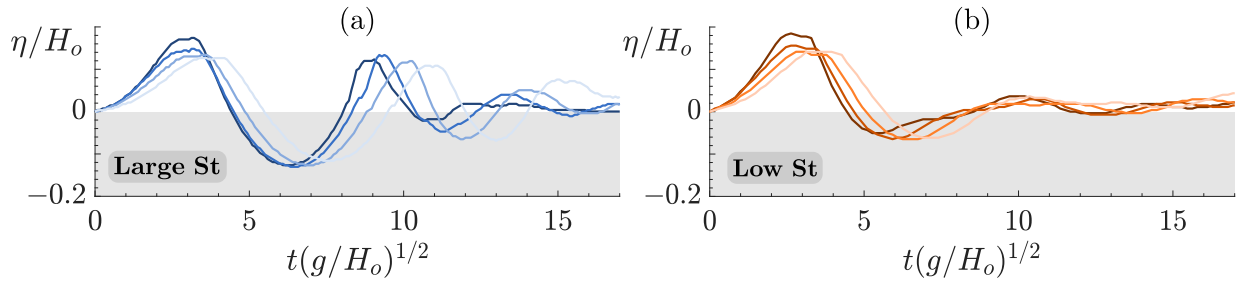

FIG. 6. Normalized free surface height η/H_o as a function of the normalized time $t(g/H_o)^{1/2}$, at $x/H_o = 3,\ 4,\ 5$ and 6 (from dark to light colors), for (a) large St [dense-inertial regime: $(Re,\ St) = (7 \times 10^4,\ 71)$] and (b) low St [dense-viscous regime: $(Re,\ St) = (561,\ 2 \times 10^{-3})$]. The initial time is defined as the time at which the first wave reaches the corresponding location.

In order to quantify these changes in the wave train profiles, the energy of the leading wave, i.e. the first positive crest, and the energy of the entire wave train, i.e. the leading and following waves, are estimated as $\widehat{E}_w = \rho_f g W c \int_0^T \eta^2 dt$ and $E_w = \rho_f g W c \int_0^\infty \eta^2 dt$, respectively. Here, the channel width is $W = 0.2$ m, the wave velocity is set to $c = 1$ m.s^{-1}

according to experimental results (more details given in Appendix C), and T is the period of the first positive crest. These energy relationships are based on the assumption of an equal distribution between potential and kinetic energy, which is true for linear waves [49] and has long been considered as a good assumption for impulse waves far enough from the shoreline [2, 6, 50]. Other studies have also reported different energy distributions [9, 51], but in the absence of further information the assumption of energy equipartition is preferred here.

First, both $\widehat{E}_w$ and E_w vary with the Stokes number St [semitransparent and opaque squares, respectively, in Fig. 7(a)]. In particular, the leading wave energy $\widehat{E}_w$, relative to the initial potential energy $E_g = mg(H_o + 2H_i/3)$ of the granular mass, decreases from 4% to 2.5% with increasing St [semitransparent squares, in Fig. 7(a)]. This observation is in qualitative agreement with the small decrease of the first wave amplitude reported previously [Fig. 4(c)]. On the other hand, the total wave train energy E_w is increased from 5% to 8% with St [opaque squares, in Fig. 7(a)], consistent with the range of $E_w/E_g \approx 1\% - 10\%$ usually reported in the literature [4, 6, 52, 53].

The difference in energy transfer from the granular mass between the leading wave and the total wave train can be quantified by the energy ratio $\widehat{E}_w/E_w$ [Fig. 7(b)]. Surprisingly, all data collapse on a sigmoidal-shaped master curve depending only on St [gray solid line, in Fig. 7(b)]. This representation also suggests two asymptotic values of $\widehat{E}_w/E_w$, at low and large St. When St is small, almost all the energy of the granular mass transferred to the free surface is contained in the first, largest wave, and secondary waves are almost nonexistent behind it, i.e., $\widehat{E}_w/E_w \approx 0.75$. The wave generation is therefore related solely to the impact process of a nearly impermeable granular flow, while transient granular deposition along the incline and near the free surface over a long period dissipates the oscillation, and hence the wave train. By contrast, at large St, the permeable granular flow reaches quickly the bottom, which allows oscillation of the free surface, and thus a significant wave train relative to the leading wave with an energy ratio of $\widehat{E}_w/E_w \approx 0.35$.

These results reveal a surprising dichotomy between the energy of the leading wave and that of the total wave train with the Stokes number St. This strengthens the assumption that the Stokes number St characterizes different physical processes in this system, including liquid percolation into the granular material as well as inertia of the granular collapse.

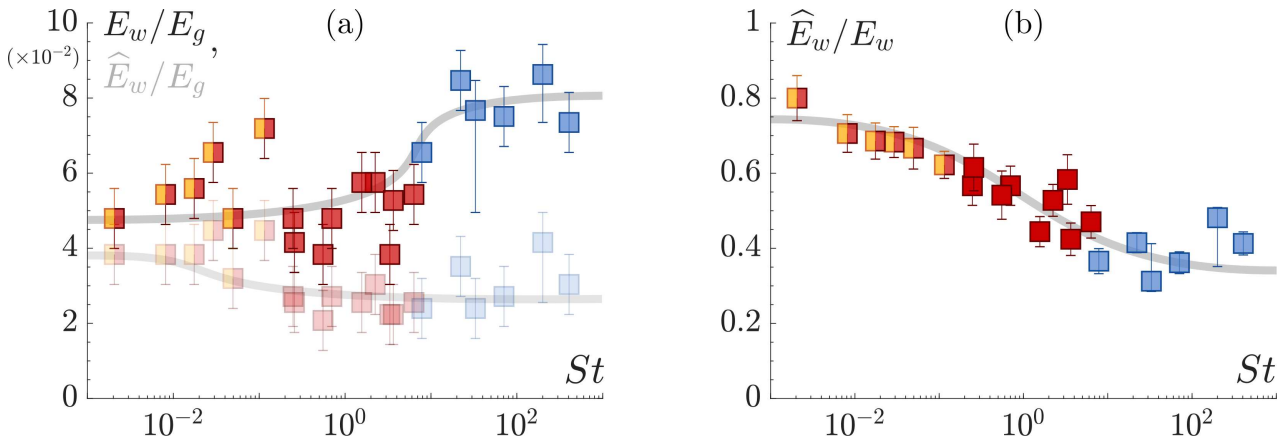

FIG. 7. (a) Energy of the total wave train E_w (opaque squares) and of the leading wave $\widehat{E}_w$ (semitransparent squares), normalized by the initial potential energy E_g of the granular mass, vs the Stokes number St. (b) Energy ratio $\widehat{E}_w/E_w$ vs St. Legend of symbol colors is given in Fig. 3. Solid lines are guides for the eyes.

CONCLUSION

This study investigates the influence of grain-liquid interactions, and especially those related to viscous dissipation, on landslide-tsunami generation through original laboratory experiments of dry granular masses of variable granulometry, collapsing into a liquid of variable viscosity. One of the main results is the wealth of collapse dynamics and deposition of the granular medium below the free surface, which are discussed in light of the flow Reynolds number Re and the Stokes number St comparing flow and grain inertia, respectively, to viscous dissipation of the liquid. Three distinct regimes are identified - dense-inertial, dilute-inertial and dense-viscous regimes - and then rationalized in the (Re, St) plane. The two inertial regimes consist of relatively rapid and distant propagation, in either a dense or dilute state, of granular avalanches in the liquid. They represent the expected situations in nature as the Stokes number St can vary considerably with the grain size, while keeping large Re. In contrast, the dense-viscous regime is characterized by a surprising arrest of the granular mass along the plane, the inclination of which exceeds the angle of repose of granular materials, with a possible lift-off at the front. This remarkable behavior is attributed to the additional viscous stresses exerted on the granular matrix due to liquid percolation, accompanied by a slow release of the air initially trapped in the granular medium. Although

collapse dynamics and deposition differ strongly between these different regimes, they do not affect significantly the characteristics of the leading and largest wave, which suggests that its generation is mainly controlled by subaerial flow conditions. The small decrease of the wave amplitude reported with St is probably associated with liquid percolation at the impact. Then, these results allow to conclude that large depositional runouts beneath the water surface are not necessarily associated with large-amplitude tsunamis. A detailed analysis further reveals that the immersed dynamics of dense granular collapse regimes mainly contributes to the total energy transferred to the free-surface, i.e., to the wave train and not to the leading wave, resulting in different waveforms. The energy ratio between the leading wave and the total wave train is thus shown to be directly dependent on the Stokes number St, suggesting different cases from an almost unique leading wave to successive waves of similar amplitudes, at low and large St, respectively. In conclusion, this study provides evidence on the importance of considering granular-liquid interaction for a better description of the shape of generated impulse waves by experimental granular flows, while offering a new type of benchmark for numerical models.

ACKNOWLEDGMENTS

We acknowledge the ANR (RAVEX Project No. ANR-16-CE03-0002) and CNRS/IRD MITI (TAnGENt project) programs for financial support. This is ClerVolc contribution n°671.

Appendix A: Quasistatic granular deposits

In the present study, the grain size is varied to investigate the role of grain-fluid interaction on wave generation, collapse dynamics, and depositional morphology of a granular mass entering a liquid. Behind the dissipative processes associated with the liquid, granular deposits can also result from various basal and internal friction due to the properties of granular materials. In order to quantify the relative importance of such effects in these experiments, the deposition characteristics of quasistatic granular collapses are estimated for all granular materials used.

In that sense, quasistatic granular collapse experiments consist in releasing a granular

mass of $m = 2\,\mathrm{kg}$, initially located along the incline and just above the smooth bottom, by moving manually and horizontally a vertical plate in a time much larger than the free-fall timescale $T_{FF} = (2H_i/g)^{1/2}$ [54], until a final deposit is obtained. To ensure that electrostatic effects and humidity do not affect the results for small grains, some experiments are carried out in air and water.

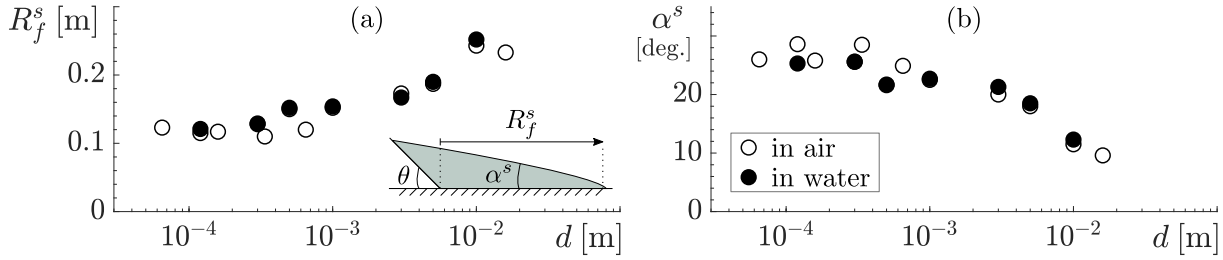

FIG. 8. Dependency on d of the (a) runout R_f^s and (b) angle α^s of deposits for quasistatic granular collapses.

The final morphology of quasistatic granular collapses can be described by a triangular shape defined by its longitudinal extension, i.e. the runout R_f^s, and its deposition angle α^s [see sketch, in Fig. 8(a)]. It turns out that both quantities depend on the grain size d, especially when d is large (Fig. 8). More precisely, the runout R_f^s increases and the deposition angle α^s decreases with increasing d, which implies a more elongated granular deposit. Mention that these opposite trends can be explained by the relationship $R_f^s/R_i = (a/\tan\alpha^s - 1)^{1/2}$ derived from mass conservation for a triangular-shaped deposit. Because of this observation, the runout R_f and the maximum local angle α_ℓ of granular deposits are always normalized by the values obtained for quasistatic granular collapses in order to avoid any misinterpretation of the results. Note that, although the ambient fluid does not modify significantly the quantitative values of R_f^s and α^s, those obtained in water are used when available.

Appendix B: Granular stabilization induced by liquid percolation

As observed in this study, the viscous-dominated collapse regime, called dense-viscous regime, is characterized by a sudden stop of the granular mass along the slope after entering the liquid, forming a transient granular deposit at a critical depth from the free surface [Fig.

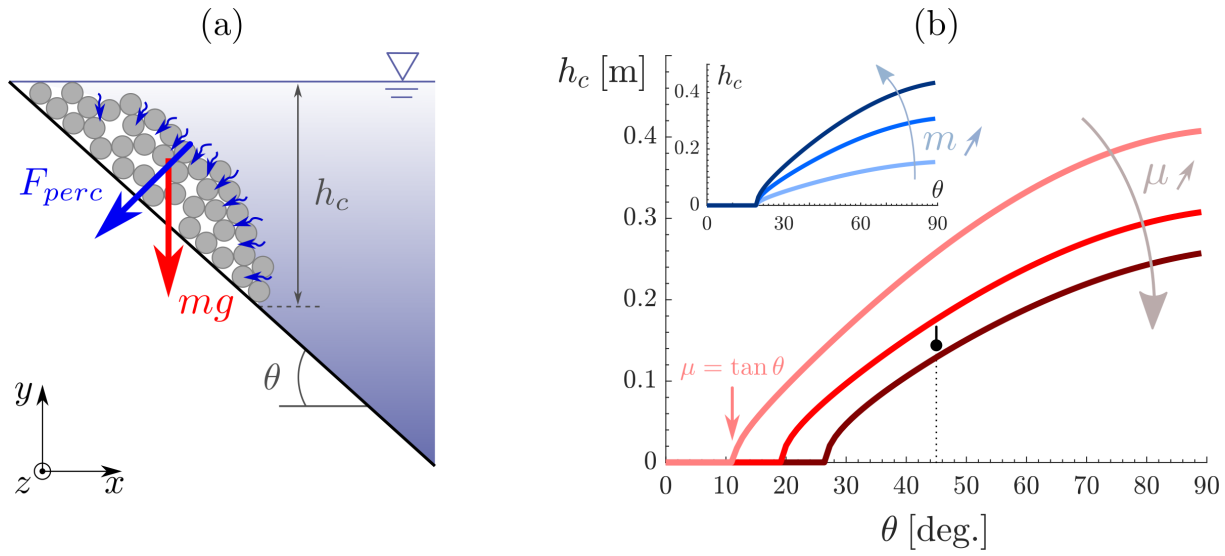

FIG. 9. (a) Sketch of the transient granular deposit, subjected to the force of gravity and liquid percolation, along the inclined plane, obtained in dense-viscous regime. (b) Prediction of critical stopping depth h_c [Eq. B3] vs slope angle θ, for different basal friction coefficients $\mu = 0.2,\ 0.35$ and 0.5 (from light to dark red) and different granular masses $m = 0.5,\ 2$ and 4 kg (inset, from light to dark blue). The default parameters are $\mu = 0.35$, $m = 2$ kg, $\phi = 0.6$, $\rho_f = 1000$ kg.m^{-3} and $W = 0.2$ m, according to this study. The black circle corresponds to $h_c = H_o = 14.5$ cm, while the error bar indicates the critical height of $h_c = 16.5$ cm estimated from the experiment with a larger water depth [47].

9(a)]. In the following, we discuss this granular stabilization based on a minimal model that provides clues for a better understanding of this mechanism.

First, this singular behavior is attributed to additional stresses applied to the granular skeleton due to liquid percolation, which can be written as

$$mg\sin\theta = \mu(mg\cos\theta + F_{perc}), \tag{B1}$$

where μ is the basal friction coefficient and F_{perc} is the liquid percolation force. In Eq. B1, left and right terms represent the gravitational driving force and the dissipative basal friction force induced by gravity and liquid percolation, respectively, the latter being assumed perpendicular to the inclined plane. Based on qualitative observations of the experiments, it is also assumed that the percolation timescale is much larger than the time needed for the grains to enter the liquid and stop along the inclined plane, which means that the

dynamics of the percolation process can be ignored. Now, let us consider that the percolation force is related to the hydrostatic pressure, which acts at the air-liquid interface on the granular medium, then fully transmitted to the bottom. In this way, there is no mention of a mechanism preventing liquid percolation, which is attributed here to viscous effects at the grain scale, whereas other processes (e.g., capillarity) could also be invoked. This leads to

$$F_{perc} = \int_0^{h_c} \frac{\phi \rho_f g W y}{\sin\theta} dy = \frac{\phi \rho_f g W {h_c}^2}{2 \sin\theta}. \tag{B2}$$

Finally, substituting Eq. B2 in Eq. B1, the critical depth h_c, at which the granular mass is expected to arrest on the slope, is obtained as

$$h_c = \left[\left(\frac{\tan\theta}{\mu} - 1 \right) \frac{2m \sin\theta}{\phi \rho_f W} \right]^{1/2}. \tag{B3}$$

First considering the parameters of this study, namely $m = 2$ kg, $\theta = 45°$, $\phi = 0.6$, $\rho_f = 1000$ kg.m^{-3} and $W = 0.2$ m, and assuming a basal friction coefficient $\mu = \tan 28°$ according to the deposit angle α^s obtained for small d [Fig. 8(b)], one obtains a critical stoppping depth of $h_c \approx 12$ cm, in fairly good agreement with the experiments. Indeed, the granular mass is observed experimentally to arrest approximately at the slope break, i.e. $h_c \approx H_o = 14.5 \pm 0.5$ cm [Fig. 2(c)], while this critical depth remains grossly unchanged with increasing H_o (see movie 5 [47]). This proposed model also captures the fact that, for $\tan\theta \leq \mu$, liquid percolation is not required to form a granular deposit along the incline, as expected for dry granular materials [Fig. 9(b)]. For $\tan\theta > \mu$, Eq. B3 predicts that increasing the slope angle θ and granular mass m promote larger critical depths h_c, which is consistent with a more important driving contribution of gravity. Finally and as expected, increasing frictional dissipation with the basal friction coefficient μ helps to reduce the runout of transient granular deposits [Fig. 9(b)]. Nevertheless, some caution should be exercised with this minimal model because it is based on several assumptions not tested experimentally. Moreover, it does not take into account the dynamics of liquid percolation into the granular material and the physical mechanism responsible of its delay. Finally, it implies that the collapse dynamics remains unchanged for steeper slopes and larger masses, which must be assessed by dedicated studies.

Appendix C: Wave propagation velocity

In Sec. V of the paper, the energy of the leading wave and of the total wave train are estimated from the temporal evolution of the free surface. In both cases, the wave propagation velocity should be known, and it has therefore been estimated from the temporal evolution of the wave amplitude position as $c = dx_w/dt$ [Fig. 10(a)]. At least for the first and second waves, the propagation velocity is approximately equal to $c = 1\ \mathrm{m.s^{-1}}$ [Fig. 10(b)]. The propagation velocity is slightly larger for the leading wave (closed circles) than for the second wave (opened circles). This value corresponds well to the typical velocity of linear gravity waves in shallow water, although it overestimates slightly the propagation velocity of waves [inset, in Fig. 10(b)]. For this reason, the propagation velocity is set to $c = 1\ \mathrm{m.s^{-1}}$ for estimating the wave energy.

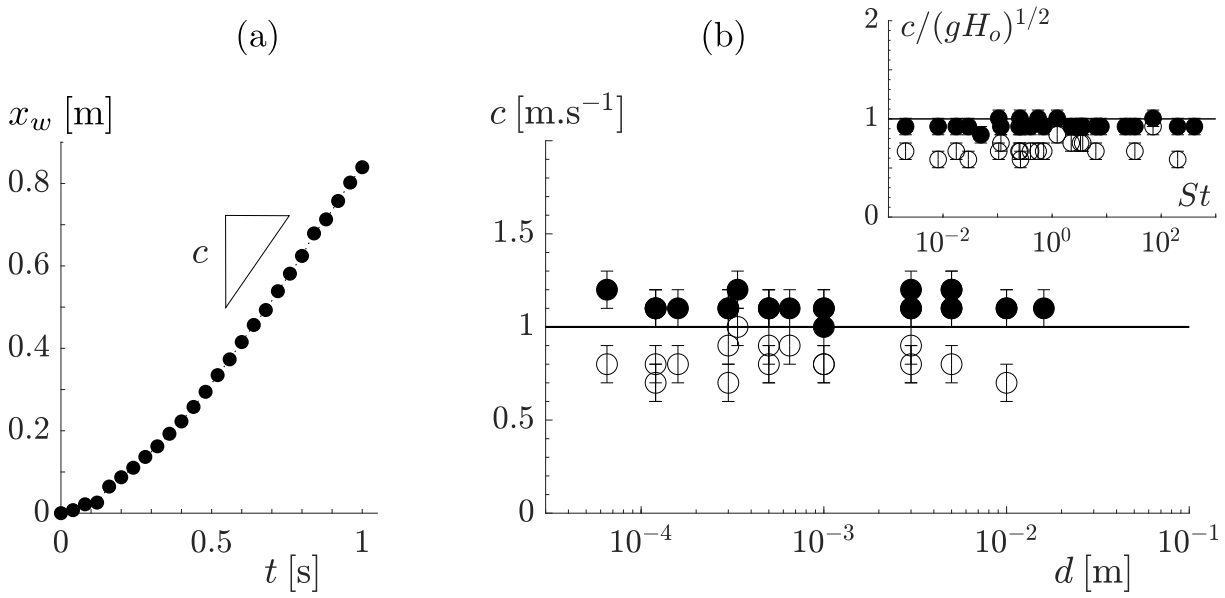

FIG. 10. (a) Typical propagation of a leading wave - $(Re,\ St) = (8 \times 10^3,\ 7.8)$. (b) Propagation velocity of the first (closed circles) and second (opened circles) waves as a function of grain diameter. (Inset) Wave velocity normalized by the typical velocity $(gH_o)^{1/2}$ of linear gravity waves in shallow water vs St.

[1] R. Delannay, A. Valance, A. Mangeney, O. Roche, and P. Richard, Granular and particle-laden flows: from laboratory experiments to field observations, J. Phys. D **50**, 053001 (2017).

[2] H. M. Fritz, W. H. Hager, and H.-E. Minor, Near field characteristics of landslide generated impulse waves, J. Waterway, Port, Coast. Ocean Eng. **130**, 287 (2004).

[3] V. Heller and W. H. Hager, Impulse product parameter in landslide generated impulse waves, J. Waterway, Port, Coast. Ocean Eng. **136**, 145 (2010).

[4] S. Viroulet, A. Sauret, and O. Kimmoun, Tsunami generated by a granular collapse down a rough inclined plane, EPL **105**, 34004 (2014).

[5] E. K. Lindstrøm, Waves generated by subaerial slides with various porosities, Coast. Eng. J. **116**, 170 (2016).

[6] G. Zitti, C. Ancey, M. Postacchini, and M. Brocchini, Impulse waves generated by snow avalanches: Momentum and energy transfer to a water body, J. Geophys. Res. **121**, 2399 (2016).

[7] G. S. Miller, W. Andy T., R. P. Mulligan, and S. McDougall, Tsunamis generated by long and thin granular landslides in a large flume, J. Geophys. Res. **122**, 653 (2017).

[8] A. Bougouin, R. Paris, and O. Roche, Impact of fluidized granular flows into water: Implications for tsunamis generated by pyroclastic flows, J. Geophys. Res. Solid Earth **125**, e2019JB018954 (2020).

[9] M. Robbe-Saule, C. Morize, R. Henaff, Y. Bertho, A. Sauret, and P. Gondret, Experimental investigation of tsunami waves generated by granular collapse into water, J. Fluid Mech. **907**, A11 (2021).

[10] B. Ataie-Ashtiani and A. Nik-Khah, Impulsive waves caused by subaerial landslides, Env. Fluid Mech. **8**, 263 (2008).

[11] C.-H. Lee and Z. Huang, Effects of grain size on subaerial granular landslides and resulting impulse waves: Experiment and multi-phase flow simulation, Landslides **19**, 137 (2022).

[12] M. Rauter, S. Viroulet, S. S. Gylfadóttir, W. Fellin, and F. Løvholt, Granular porous landslide tsunami modelling–the 2014 Lake Askja flank collapse, Nat. Commun. **13**, 1 (2022).

[13] R. L. Wiegel, Laboratory studies of gravity waves generated by the movement of a submerged body, Trans. Am. Geophys. Union **36**, 759 (1955).

[14] L. Law and A. Brebner, On water waves generated by landslides, in *Proc. Third Australas. Conf. Hydraul. Fluid Mech., Sydney, Australia* (1968).

[15] J. W. Kamphuis and R. J. Bowering, Impulse waves generated by landslides, in *Proc. 12th Coast. Eng. Conf., New York, United States* (1970).

[16] P. Heinrich, Nonlinear water waves generated by submarine and aerial landslides, J. Waterway, Port, Coast. Ocean Eng. **118**, 249 (1992).

[17] J. J. Monaghan and A. Kos, Scott Russell's wave generator, Phys. Fluids **12** (2000).

[18] J. S. Walder, P. Watts, O. E. Sorensen, and K. Janssen, Tsunamis generated by subaerial mass flows, J. Geophys. Res. **108** (2003).

[19] B. Huang, Q. Zhang, J. Wang, C. Luo, X. Chen, and L. Chen, Experimental study on impulse waves generated by gravitational collapse of rectangular granular piles, Phys. Fluids **32**, 033301 (2020).

[20] M. A. Cabrera, G. Pinzon, W. A. Take, and R. P. Mulligan, Wave generation across a continuum of landslide conditions from the collapse of partially submerged to fully submerged granular columns., J. Geophys. Res. Oceans **125**, e2020JC016465 (2020).

[21] W. Sarlin, C. Morize, A. Sauret, and P. Gondret, Nonlinear regimes of tsunami waves generated by a granular collapse, J. Fluid Mech. **919**, R6 (2021).

[22] N. H. T. Nguyen, Collapse of partially and fully submerged granular column generating impulse waves: An empirical law of maximum wave amplitude based on coupled multiphase fluid-particle modeling results, Phys. Fluids **34**, 013310 (2022).

[23] A. Darvenne, S. Viroulet, and L. Lacaze, Physical model of landslide-generated impulse waves: Experimental investigation of the wave-granular flow coupling, J. Geophys. Res. Oceans **129**, e2024JC021145 (2024).

[24] A. Bougouin, R. Paris, O. Roche, M. Siavelis, and A. Pawlak Courdavault, Tsunamis generated by pyroclastic flows: Experimental insights into the effect of the bulk flow density, Bull. Volcanol. **86**, 35 (2024).

[25] W. Sarlin, C. Morize, A. Sauret, and P. Gondret, From granular collapses to shallow water waves: A predictive model for tsunami generation, Phys. Rev. Fluids **7**, 094801 (2022).

[26] Q. Kriaa, S. Viroulet, and L. Lacaze, Modeling of impulse waves generated by a viscous collapse in water, Phys. Rev. Fluids **7**, 054801 (2022).

[27] R. P. Mulligan and W. A. Take, On the transfer of momentum from a granular landslide to a water wave, Coast. Eng. **125**, 16 (2017).

[28] E. Treflik-Body, E. Steel, W. A. Take, and R. P. Mulligan, Large-scale physical modeling of wave generation and runup on slopes from the collapse of partially and fully submerged granular columns, J. Geophys. Res. Oceans **129**, e2023JC020689 (2024).

[29] G. K. Bullard, R. P. Mulligan, A. Carreira, and W. A. Take, Experimental analysis of tsunamis generated by the impact of landslides with high mobility, Coast. Eng. **152**, 103538 (2019).

[30] M.-L. Yu and C.-H. Lee, Multi-phase-flow modeling of underwater landslides on an inclined plane and consequently generated waves, Adv. Water Resour. **133**, 103421 (2019).

[31] A. Freundt, Entrance of hot pyroclastic flows into the sea: Experimental observations, Bull. Volcanol. **65**, 144 (2003).

[32] S. R. Allen, A. Freundt, and K. Kurokawa, Characteristics of submarine pumice-rich density current deposits sourced from turbulent mixing of subaerial pyroclastic flows at the shoreline: Field and experimental assessment, Bull. Volcanol. **74**, 657 (2012).

[33] A. Bougouin, R. Paris, O. Roche, and H. E. Huppert, Experimental insights on the propagation of fine-grained geophysical flows entering water, J. Geophys. Res. Oceans **126**, e2020JC016838 (2021).

[34] M. Pilvar, M. J. Pouraghniaei, and A. Shakibaeinia, Two-dimensional sub-aerial, submerged, and transitional granular slides, Phys. Fluids **31**, 113303 (2019).

[35] A. M. Cervantes-Álvarez, Y. Y. Escobar-Ortega, A. Sauret, and F. Pacheco-Vázquez, Air entrainment and granular bubbles generated by a jet of grains entering water, J. Colloid Interf. Sci. **574**, 285 (2020).

[36] G. Saingier, A. Sauret, and P. Jop, Falling jet of dry granular material in water, J. Fluid Mech. **916**, A34 (2021).

[37] S. T. Grilli, M. Shelby, O. Kimmoun, G. Dupont, D. Nicolsky, G. Ma, J. T. Kirby, and F. Shi, Modeling coastal tsunami hazard from submarine mass failures: effect of slide rheology, experimental validation, and case studies off the US East Coast, Nat. Hazards **86**, 353 (2017).

[38] A. Bougouin, Etude expérimentale de l'effondrement d'une colonne fluide-grains, Institut National Polytechnique de Toulouse **Ph.D. thesis** (2017).

[39] See supplemental material at http://link.aps.org/supplemental/10.1103/physrevfluids.9.124302 for the summary table of experiments (ExpSummaryTable.ods).

[40] I. R. Ionescu, A. Mangeney, F. Bouchut, and O. Roche, Viscoplastic modeling of granular column collapse with pressure-dependent rheology, J. Non-Newtonian Fluid Mech. **219**, 1 (2015).

[41] S. Courrech du Pont, P. Gondret, B. Perrin, and M. Rabaud, Granular avalanches in fluids, Phys. Rev. lett. **90**, 044301 (2003).

[42] A. Bougouin and L. Lacaze, Granular collapse in a fluid: Different flow regimes for an initially dense-packing, Phys. Rev. Fluids **3**, 064305 (2018).

[43] See Supplemental Material at http://link.aps.org/supplemental/10.1103/physrevfluids.9.124302 for Movie 1 showing the dense-inertial regime ($d = 5\,\mathrm{mm}$, $\eta_f = 1\,\mathrm{mPa.s}$).

[44] See Supplemental Material at http://link.aps.org/supplemental/10.1103/physrevfluids.9.124302 for Movie 2 showing the dilute-inertial regime ($d = 120\,\mu\mathrm{m}$, $\eta_f = 1\,\mathrm{mPa.s}$).

[45] See Supplemental Material at http://link.aps.org/supplemental/10.1103/physrevfluids.9.124302 for Movie 3 showing the dense-viscous regime without lift-off ($d = 5\,\mathrm{mm}$, $\eta_f = 126\,\mathrm{mPa.s}$).

[46] See Supplemental Material at http://link.aps.org/supplemental/10.1103/physrevfluids.9.124302 for Movie 4 showing the dense-viscous regime with lift-off ($d = 120\,\mu\mathrm{m}$, $\eta_f = 126\,\mathrm{mPa.s}$).

[47] See Supplemental Material at http://link.aps.org/supplemental/10.1103/physrevfluids.9.124302 for Movie 5 showing the evidence of the avalanche stopping on the incline in the dense-viscous regime ($H_o = 25\,\mathrm{cm}$, $d = 337\,\mu\mathrm{m}$, $\eta_f = 1\,\mathrm{mPa.s}$).

[48] P. Mcleod, S. Carey, and R. S. J. Sparks, Behaviour of particle-laden flows into the ocean: Experimental simulation and geological implications, Sedimentology **46**, 523 (1999).

[49] B. Le Méhauté, *An introduction to hydrodynamics and water waves* (Springer, New York, 1976).

[50] F. Mohammed and H. M. Fritz, Physical modeling of tsunamis generated by three-dimensional deformable granular landslides, J. Geophys. Res. **117**, C11015 (2012).

[51] V. Heller, *Landslide generated impulse waves: Prediction of near field characteristics*, Ph.D. thesis, ETH Zurich (2007).

[52] L. Clous and S. Abadie, Simulation of energy transfers in waves generated by granular slides, Landslides **16**, 1663 (2019).

[53] S. Yavari-Ramshe and B. Ataie-Ashtiani, On the effects of landslide deformability and initial submergence on landslide-generated waves, Landslides **16**, 37 (2019).

[54] W. Sarlin, C. Morize, A. Sauret, and P. Gondret, Collapse dynamics of dry granular columns: From free-fall to quasistatic flow, Phys. Rev. E **104**, 064904 (2021).